# Intuitive Control of Low-Energy Magnetic Excitations via Directed Dipolar Interactions in a Series of Er(III)-Based Complexes

Angelica P. Orlova, Jeremy D. Hilgar, Maximilian G. Bernbeck, Milan Gembicky, Jeffrey D. Rinehart\*

Department of Chemistry and Biochemistry, University of California, San Diego, La Jolla, California 92093, United States.

**ABSTRACT:** Dipolar coupling is rarely invoked as a driving force for slow relaxation dynamics in lanthanide-based single-molecule magnets, though it is often the strongest mechanism available for mediating inter-ion magnetic interactions in such species. Indeed, for multinuclear lanthanide complexes, the magnitude and anisotropy of the dipolar interaction can be considerable given their ability to form highly directional, high-moment ground states. Herein we present a mono-, di-, and tri-nuclear erbium-based single-molecule magnet sequence,  $([Er - TiPS_2COT]^+)_n$  (n = 1 - 3), wherein a drastic reduction in the allowedness of magnetic relaxation pathways is rationalized within the framework of the dipole-dipole interactions between angular momentum quanta. The resulting design principles for multinuclear molecular magnetism arising from intramolecular dipolar coupling interactions between highly anisotropic magnetic states present a nuanced justification of the relaxation dynamics in complex manifolds of individual quantized transitions. Experimental evidence for the validity of this model is provided by coupling the relaxation dynamics to an AC magnetic field across an unprecedented frequency range for molecular magnetism  $(10^3 - 10^{-5} \text{ Hz})$ . The combination of slow dynamics and multiple, low-energy transitions leads to a number of noteworthy phenomena, including a lanthanide single-molecule magnet with three well-defined relaxation processes observable at a single temperature.

#### INTRODUCTION

The field of molecular magnetism seeks synthetic control over the temporal and spatial flow of magnetic information at the molecular level. One aspect of this control has been the manipulation of the characteristic magnetic relaxation timescale away from that of isotropic paramagnetism.<sup>1</sup> In this field, known as Single-Molecule research Magnetism (SMM), perturbations to a bistable spin ground state are used to generate an energy barrier which prevents direct relaxation between opposite orientations of the magnetic moment.<sup>2-4</sup> Advances synthetic technique and understanding in this field have led to slowing of paramagnetic relaxation by a factor of 109 or more at liquid nitrogen temperatures.<sup>5</sup> In recent years, the challenge of manipulating the relaxation time has grown more nuanced as the many underlying factors controlling magnetic relaxation have become better understood.6-10 Molecular-level magnetic design has many interesting prospects, especially if the design principles form the basis of a building-block approach to more complex or hierarchical magnetic structures.

Two of the major challenges in rational assembly of magnetic building units are (1) maintenance of the desired magnetic properties under the mutable electronic structure conditions of assembly and (2) predicting the net interaction caused by a manifold of magnetic interaction pathways. To overcome the first challenge, we have used the erbium(III) cyclooctatetraenide-based building unit ([ErCOT]+)

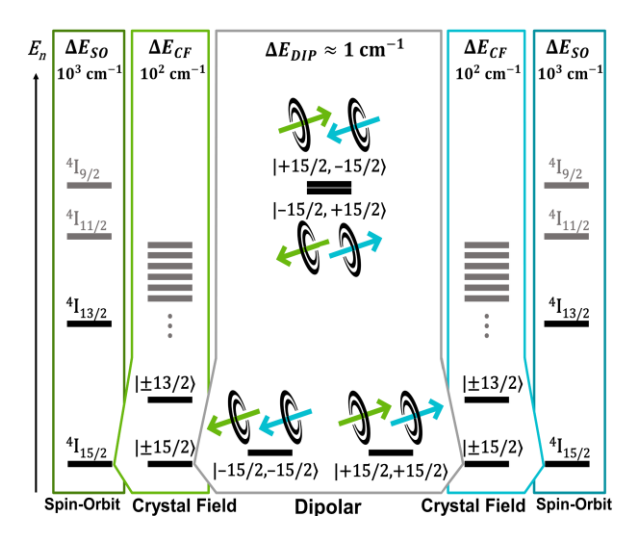


Figure 1. Idealized perturbative scheme for a dinuclear interaction between two magnetic centers, each with the general electronic structure of the [ErCOT]+ unit. The center energy splitting represents a pure magnetic dipolar interaction between pseudo-spin  $\tilde{s}=\frac{1}{2}$  Kramers doublets with  $g_x=g_y=0$ . Green and blue arrows represent singleion anisotropy axes with the arrow direction representing the composition of magnetic ground state orientations for individual eigenstates.

which can function as a reliable source of axial anisotropy in the presence of a wide range of ligands. Fundamentally, [ErCOT]+ directs single-ion anisotropy by a combination of favorable crystal field interactions between Er³+ and COT²- and minimal energy-level restructuring from the preferred tripodal arrangement of the remaining coordination sites.¹¹-¹6 The [ErCOT]+ building unit offers a tangible, versatile, synthetic connection between real-space and spin-space for the design of

magnetic structures that largely conserve single-ion anisotropy oriented along the Er-COT vector  $(\vec{r}_1)$ .

In this work, we extend our approach to demonstrate how control over the single-ion

anisotropy axis can be leveraged for chemical intuition over more complex interactions in molecular clusters. For this study, the solubility and steric bulk of the 1.4bis(triisopropylsilyl)cyclooctatetraenide (TiPS<sub>2</sub>COT<sup>2-</sup>) anion are utilized to direct the singleion anisotropy of Er3+ in mono-, di-, and trinuclear complexes. These three molecules. progressively more complex intramolecular interactions, are used to demonstrate how a simple heuristic (Figure 1) yields a structurally intuitive model that is surprisingly consistent with both magnetic and computational data. These results highlight that while the dipole-dipole magnetic interaction is often considered inconsequential or detrimental to control of magnetic relaxation, in properly controlled cases, 17 it can drastically and reliably alter the allowedness of transitions, presenting a reliable means of control over complex low-energy state manifolds.

#### **EXPERIMENTAL**

As a basis for our analysis of molecular magnetic relaxation at the anisotropic dipolar limit, we synthesized mononuclear  $(n^8-1.4$ bis(triisopropylsilyl)cyclooctatetraenyl)-iodobis(tetrahydrofuran)-erbium (1), dinuclear bis( $n^2$ iodo)-bis( $(\eta^{8}-1,4-$ 

bis(triisopropylsilyl)cyclooctatetraenyl)tetrahydrofuran-erbium) (2), and trinuclear ( $\mu_2$ iodo)-bis( $\mu_3$ -iodo)-tris( $\eta^8$ -1,4-

bis(triisopropylsilyl)cyclooctatetraenyl-erbium)

(3). Briefly, synthesis of 1 is achieved by addition of dipotassium 1,4-bis(triisopropylsilyl)cyclooctatetraenide (K2TiPS2COT) to an erbium triiodide suspension (-30 °C, THF). After extraction into THF and filtration, a vapor diffusion with pentane yields pink needles of 1. Dissolution of 1 into benzene, and crystallization from a benzene/pentane layering yields the dinuclear complex 2, as red-orange plates. The trinuclear form, 3, is synthesized via slow addition of trimethylaluminum (TMA, −30 °C, toluene) to 1 or 2. Pentane trituration of the resulting oil, followed by crystallization out of a concentrated hexane solution  $(-30 \cdot C)$ , leads to orange crystals of 3 (Figure 2). Quantitative solid-state structural information was obtained from single-crystal X-ray diffraction data collected with a Mo anode source (Figure 2, S1-S3). Similar to analogous complexes synthesized with the unsubstituted cyclooctatetraenide  $(COT^{2-})^{13,18-29}$ , anion

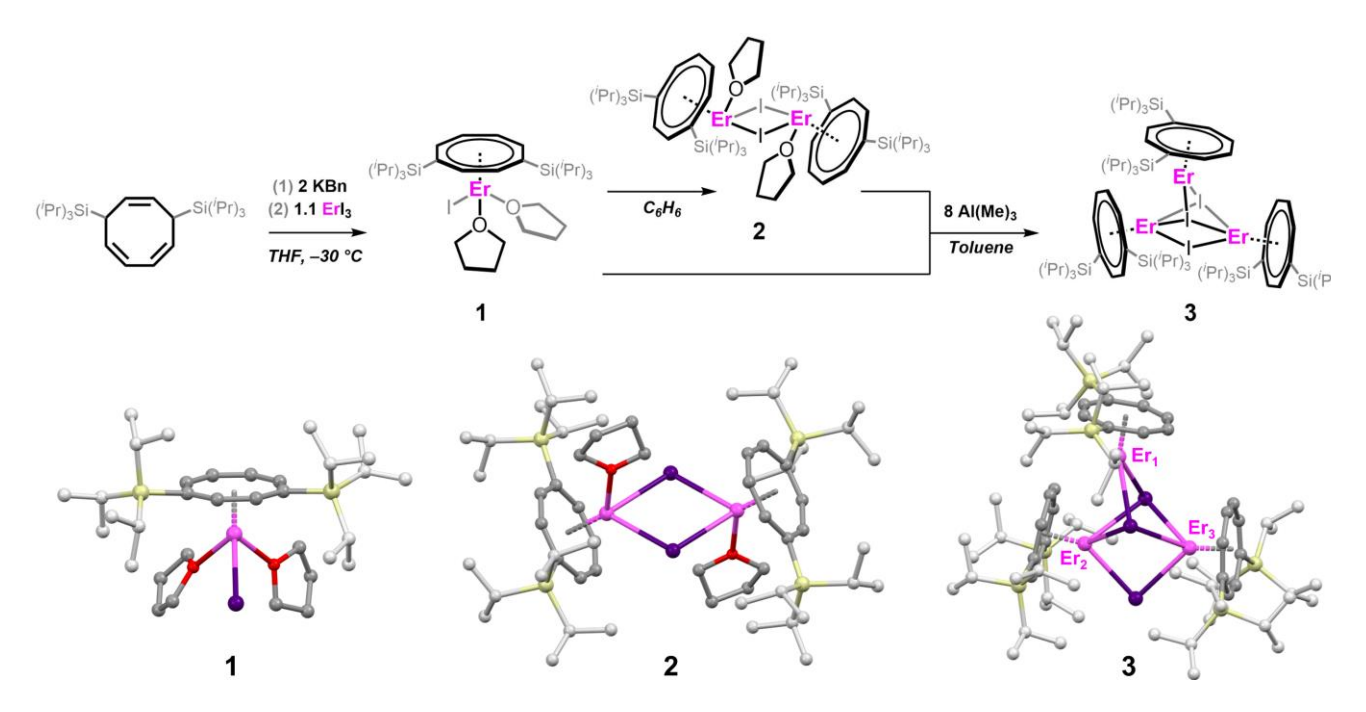


Figure 2. Synthetic scheme of 1, 2, and 3 (top). Solid states structures of 1, 2, and 3 with spheres representing erbium (light pink), iodine (purple), silicon (light yellow), oxygen (red), and carbon (gray). Hydrogen atoms have been omitted and triisopropylsilyl groups have been lightened for clarity (bottom).

mononuclear 1 and dinuclear 2 adopt piano-stool inversion-symmetric  $[\mu_2-I]_2$  geometries, respectively. Compound 3 adopts a low symmetry trinuclear structure with three crystallographically unique Er<sup>3+</sup> centers. Two Er<sup>3+</sup> centers are nearly collinear, bridged by three iodide ligands. The third erbium center is bridged by two iodide ligands and participates in a nearly orthogonal configuration in relation to the former two metal centers. Devoid of coordinating solvent, TIPS2COT2- completes the coordination sphere for each metal center. Erbium centers within 2 are separated by 4.8 Å, whereas the distances between erbium centers in 3 vary between 3.9 - 4.6 Å (Tables S1-S2). The nearest intramolecular Er-Er distances are approximately double those seen intermolecularly for both compounds.

As discussed previously,<sup>1,1,1,3</sup> the Er–COT vector  $(\vec{r}_{\perp})$  can be used as a fully structural, real-space proxy for the single-ion anisotropy axis in these compounds. As such, their magnetic behavior is befitting discussion under the lens of dipolar coupling. The magnetic dipole-dipole equation (Eq. 1) depends on magnetic moments  $(\vec{\mu})$  and the internuclear unit vector  $(\hat{n} = \vec{r}/r)$ , where r is the magnitude of  $\vec{r}$ .

$$E_{dip} = -\frac{\mu_{Bohr}^2}{r^3} \left[ 3(\vec{\mu}_1 \cdot \hat{n}_{12})(\vec{\mu}_2 \cdot \hat{n}_{12}) - \vec{\mu}_1 \cdot \vec{\mu}_2 \right]$$
(Eq. 1)

In our analysis, two structural parameters are chosen due to their connection to the dipolar term magnetic interactions (vide infra): internuclear erbium distance (r) and the angle from the projection of  $\vec{r}_{\perp}$  onto  $\vec{r}$  ( $\theta$ ; see Figures S4-S5, Tables S1-S4). These purely structural parameters provide an intuitive and simple approximation of the type of coupling expected to be present in the ground and excited dipolar states. In the discussion, these structural, real-space parameters will be used to predict and rationalize the computationally predicted (spin-space) splitting of the single-ion states by the dipole-dipole interaction and justify the nature and magnitude of the time-dependence in the magnetic results. Importantly, the success of this model demonstrates how the full versatility of synthetic design can be brought to bear on quantum challenges currently lacking a diversity of candidate materials.

# **RESULTS**

**Static Magnetic Properties.** Temperature-dependent magnetic susceptibility data were

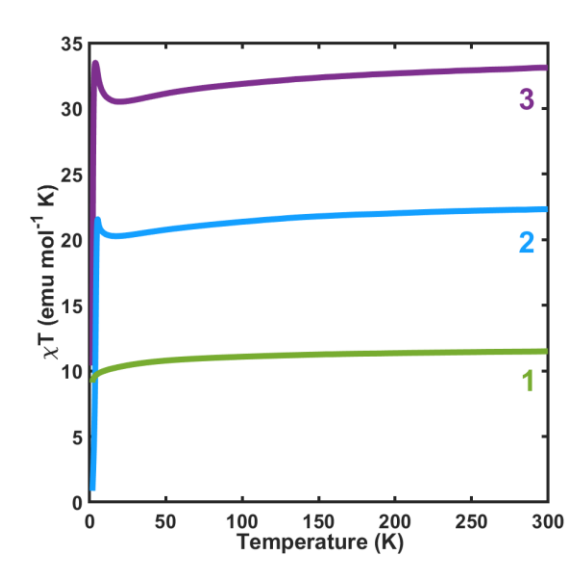


Figure 3. Zero-field cooled magnetic susceptibility data plotted as  $\chi T$  vs. T for **1–3** collected between T = 2–300 K under an applied field of H = 100 Oe.

collected on crushed microcrystalline samples between T = 2-300 K at an applied field of  $H_0 =$ 100 Oe. Field-cooled susceptibility data (FC,  $\chi_M T$ ) were collected by subjecting samples to an external field of  $H = H_0$  as the temperature was lowered to T = 2 K with subsequent data collection occurring as the temperature was incremented back up to T = 300 K. Zero-Field Cooled susceptibility data (ZFC,  $\chi_M T$ ) were collected in a similar fashion, but without the biasing field during the initial cooling. As an added precaution, active removal of remnant magnetic fields was effected prior to measurement by linearly ramping the field to H = 1 T with subsequent oscillations about H = 0 T of diminishing magnitude. Behavior of  $\chi_M T$  for **1–3** is as a susceptibility-temperature represented product  $(\chi_M T)$  to highlight deviations from Curie paramagnetism (Figure 3). Analysis of the  $\chi_M T$ product for 1-3 at T = 300 K shows nearquantitative agreement with a Landé g-factor description<sup>30</sup> of an isotropic I = 15/2 state (100.0, 97.0, and 96.0 % of the full value for**1**–**3**,respectively). As T is lowered, each data set shows a monotonic decrease in  $\chi_M T$  corresponding to thermal depopulation of higher-energy Kramers doublets of the J = 15/2 spin-orbit manifold. At low temperatures, multinuclear complexes 2-3display markedly different behavior compared to mononuclear 1. The multinuclear complexes display a sharp upturn in  $\chi_M T$  as internuclear coupling begins to dominate changes to the Boltzmann distribution. With continued lowering of temperature, the ZFC data of  $\mathbf{2} - \mathbf{3}$  reach maxima  $(2, \chi_M T = 21.6 \text{ emu K mol}^{-1}, T = 5.4 \text{ K}; 3, \chi_M T =$ 

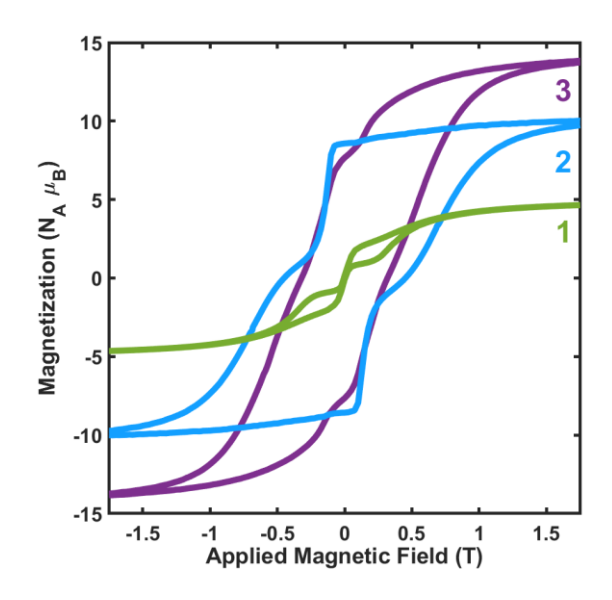


Figure 4. Isothermal magnetization of **1** (green), **2** (blue), and **3** (purple) at 2 K with  $H_c = 0,0.45$ , and 0.32 T, respectively. Data were collected at a 50 Oe s<sup>-1</sup> magnetic field sweep rate.

33.5 emu K mol<sup>-1</sup>, T=3.9 K). A divergence in FC/ZFC behavior is observed near the maxima, with both **2** and **3** displaying abrupt drops in ZFC magnetization (Figures S10, S15, S20). This behavior is indicative of magnetic blocking on the measurement timescale. The low temperature magnetism of **2** – **3** contrasts with observations for mononuclear **1**, where  $\chi_M T$  simply declines monotonically with T over the entire measurement range.

To further probe the magnetic blocking behavior, isothermal magnetization measurements were collected with a scan rate of  $dH/dt=50~{\rm Oe/s}$ . At  $T=2~{\rm K}$ , each compound reaches magnetic saturation ( $M_{sat}=5.0,10.5,{\rm and}~14.7~N_A\mu_B$  for 1-3, respectively) with applied fields above  $H=4~{\rm T}$ . Consistent with the absence of evidence for magnetic blocking in its FC/ZFC susceptibility curves, 1 displays butterfly-shaped hysteresis with negligible remanent magnetization ( $M_r=M_{H=0}=0$ ) at our scan rate. Also consistent with divergences observed in ZFC/FC  $\chi_M T$  data, 2 and 3 display open hysteresis with coercive fields of  $H_c=0.45$  and  $0.32~{\rm T}$ , respectively (Figure 4, S11, S16, S21).

**Dynamic Magnetic Properties.** Magnetic relaxation dynamics in the  $v_{AC}=10^{-1}-10^3\,\mathrm{Hz}$  regime were probed using standard AC magnetometry techniques. Additional longer-timescale relaxation dynamics  $(v_{AC}=10^{-1}-10^{-1})$ 

10<sup>-5</sup>Hz) were probed via a previously described method of coupling the magnetic relaxation response to low-frequency square-wave drive fields 5).14 Temperature and frequencydependence of the AC susceptibility response of 1-**3** is decomposed into in-phase  $(\chi'_M)$  and out-ofphase  $(\chi_M'')$  components of the molar magnetic susceptibility and fit to an extended Debye model (Equation S1), which sums up one, two, or three modified Debye functions for 1-3, respectively.31-34 This model captures inhomogeneous broadening of the relaxation distribution ( $\alpha$ ), as well as the presence of one or more characteristic relaxation times for the magnetization ( $\tau$ ). Compound 1 displays highly homogeneous relaxation, with the  $\alpha$ parameter very close to zero over a broad temperature range and a single, well-defined relaxation process (Figure S12-S14, Table S5). In contrast, multiple relaxation processes are present for 2-3 (Figure 5, AC Susceptibility; Figure 6; Arrhenius plots). Two relaxation processes were resolved within the measured range of T =9 – 14 K for 2, with subsequent merging to a single resolvable process at lower temperatures. Three distinct relaxation processes were observed for 3 from T = 14 - 17 K with the faster two merging at lower temperatures and the slowest remaining distinct down to T = 2 K (Figure 5, S17-S24, Tables S6-S7). These data are consistent with a model for multiple relaxation times of intramolecular origin proposed by Ho and Chibotaru.<sup>34</sup> Importantly, the model predicts that when multiple relaxation processes contribute significantly within frequency range, measured one parameterized as the sum of rates of individual processes (Orbach, Raman, etc.), whereas the second process will solely depend on another Orbach relaxation rate. We see this to be consistent with our experimental findings, such that the relaxation processes  $\Gamma_{2A}$  and  $\Gamma_{2B}$  (and  $\Gamma_{3A}$ ,  $\Gamma_{3B}$ ,  $\Gamma_{3C}$ ) differ in their respective Orbach regimes.

**Computational Findings.** Further understanding of the connection between the spatial arrangement of magnetic centers within each molecule and the resulting magnetic properties was garnered through computational modeling. The basic approach was to use the **OpenMolcas** computational package for ab initio calculation of the electronic structure of 1-3 including the coupling.35,36 crucial effects of spin-orbit Subsequently, the SINGLE\_ANISO module within **OpenMolcas** was employed to formulate

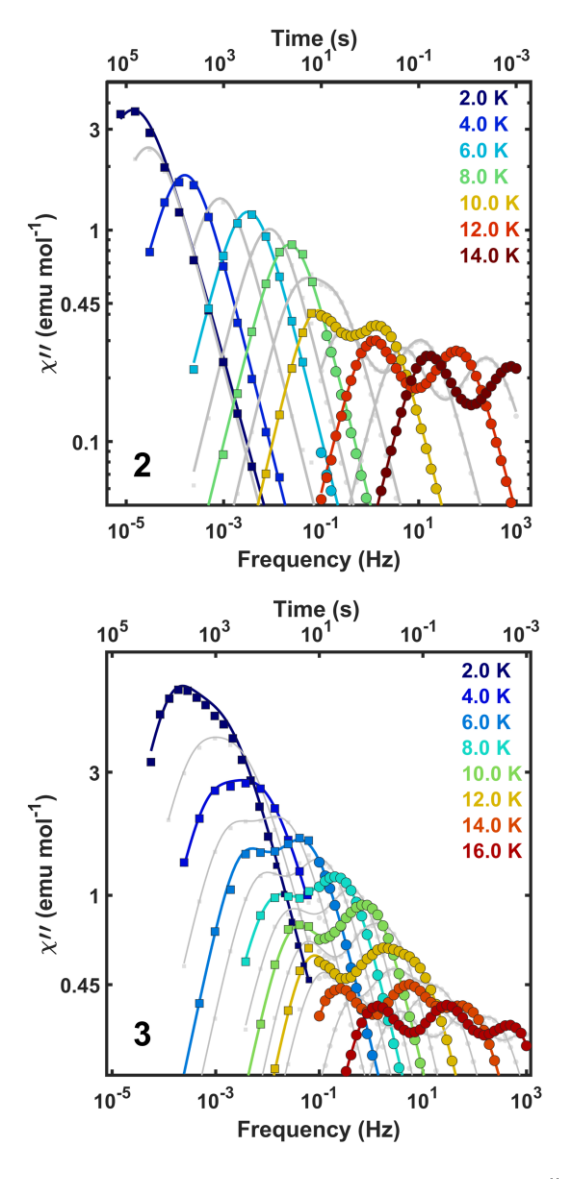


Figure 5. Plots of AC out-of-phase susceptibility  $(\chi'')$  for 2 (top) and 3 (bottom). Data points are susceptibilities measured via standard AC measurements (circles) and extracted from Fourier analysis of VSM data (squares). Lines represent fits to an extended Debye model. For clarity, odd-temperature data are grayed out.

pseudospin Hamiltonians describing the low-lying state manifold at single spin centers. For  ${\bf 1}$ , this represents a model for the magnetic behavior of the molecule, while for  ${\bf 2}-{\bf 3}$ , it represents the electronic structure of each spin center of the cluster in the absence of any coupling perturbation from other spin centers. In  ${\bf 2}-{\bf 3}$ , the POLY\_ANISO module of OpenMolcas was used to model the nature and strength of interactions between single-ion magnetic centers. To Roughly, these steps can be considered a computational realization of the heuristic perturbations introduced in Figure 1. Input structural geometries for these calculations were taken from atom position refinements against

crystallographic data and were not optimized further. As expected for a mononuclear structure based on the [ErCOT]+ building unit, 12,13,15 1 possesses a strongly axial ground state  $(KD_0; c_J | \pm M_J) = 0.98 | \pm \frac{15}{2} \rangle$ ) where  $c_J$  is the coefficient of the largest contributor from the  $M_I$ basis to the ground state Kramers doublet,  $KD_0$ . It should be noted that the axial ground state projection into real-space is anticipated by the structural parameter,  $\theta$ , discussed above, with only a minor deviation represented by the cant angle  $(\theta_{cant,1} = 1.6^{\circ}; \text{Table S9})$ . The bistable ground Kramers doublet,  $KD_0$ , is separated from the first excited doublet,  $KD_1$  (0.93|  $\pm \frac{13}{2}$ )), by a crystal field energy of 85 cm<sup>-1</sup>; the second excited Kramers doublet is found at 118 cm<sup>-1</sup> ( $KD_2$ : 0.97|  $\pm \frac{1}{2}$ ); and the third at  $163 \text{ cm}^{-1} (KD_3: 0.86 | \pm \frac{3}{2})$ ; (Figure S25, Tables S8-S10). As proof-of-concept, and to simplify further computational load, we completed identical calculations on a truncated version of 1, replacing the triisopropylsilyl groups with hydrogen atoms placed according to a standard riding model<sup>38,39</sup> (referred to as [1]). Aligning with findings, 14,40,41 symmetry-lowering previous substitutions on COT<sup>2-</sup> appear to play a negligible role in modulating the cylindrical p-electron density needed to stabilize prolate  $M_J = \pm \frac{15}{2}$  states on the Er<sup>3+</sup> ion  $(\theta_{cant,[1]} = 1.1^{\circ}; \theta_{cant,1} = 1.6^{\circ};$ Table S9). With this in mind, triisopropylsilyl groups were substituted with hydrogen atoms in the ab initio calculations for 2 and 3 placed according to a standard riding model, (hereafter referred to as [2] and [3]).

Averages of the moduli of the transition matrix elements connecting eigenstates through a Zeeman perturbation ( $\|T_{ij}\|$ ) are tabulated for states within the  $J=\frac{15}{2}$  manifold for **[1]-[3]** (Tables S10, S13, S18). As discussed in prior work,<sup>42</sup> the magnitude of the magnetic moment matrix terms correlates to the probabilities of those transitions. In this work, we will utilize the following notation in our discussion of transitions between states:

$$KD_{n,\alpha} \xrightarrow{||T_{ij}||} KD_{n,\beta} (Eq. 2)$$

where n is the KD state,  $\alpha$  and  $\beta$  are Kramers doublet components related by time-reversal, and  $||T_{ij}||$  is the average magnetic moment matrix element for that transition. As seen in [1], there is a

relatively low intrinsic probability for QTM transitions within the ground state,

$$KD_{0,\alpha} \stackrel{\longleftarrow}{\longleftrightarrow} KD_{0,\beta} \quad (Eq. 3),$$
 and first excited state, 
$$KD_{1,\alpha} \stackrel{\longleftarrow}{\longleftrightarrow} KD_{1,\beta} \quad (Eq. 4).$$

In the absence of internuclear interactions, the inversion symmetric erbium centers in **[2]** display low-energy Kramers landscapes roughly equivalent to the mononuclear compound  $\left(KD_0: 0.99 \mid \pm \frac{15}{2}\right)$ ;  $KD_1$ ,  $96 \text{ cm}^{-1}: 0.98 \mid \pm \frac{13}{2}\right)$ ;  $KD_2$ ,  $194 \text{ cm}^{-1}: 0.98 \mid \pm \frac{1}{2}\right)$ ;  $KD_3$ ,  $240 \text{ cm}^{-1}: 0.86 \mid \pm \frac{3}{2}\right)$ . A similar correlation between the electronic and physical structure is seen as well  $\left(\theta_{cant,[2]} = 1.4^{\circ}\right)$ ; Figure S26, Tables S11 - S13):

$$KD_{0,\alpha} \stackrel{\longleftarrow}{\longleftrightarrow} KD_{0,\beta} \ (Eq. 5)$$
 and 
$$KD_{1,\alpha} \stackrel{\longleftarrow}{\longleftrightarrow} KD_{1,\beta} \ (Eq. 6).$$

It's important to note that the [ErCOT]+-based anisotropy is not wholly inert to crystal field perturbations. The single iodine and two THF ligands of [1] can be expected to lead to differences in mixing terms when compared to the two iodine and one THF ligand present in [2]. Although they can be significant in excited states, these differences are minimized in dipolar coupling between  $KD_0$  states where our analysis focuses.

Several computational models of trinuclear **3** were generated utilizing complex **[3]** due to its low symmetry and three crystallographically distinct  $Er^{3+}$  centers. For each  $Er^{3+}$  center, a separate singleion calculation was completed, the results of which yielded three distinct energy manifolds (Figure S28-S30, Tables S16-S18). All three centers exhibit nearly pure ground and first excited Kramers doublets with state mixing in further excited states as expected for  $[ErCOT]^{+}$ -based subunits. The robust nature of the  $[ErCOT]^{+}$  anisotropy building unit to crystal field perturbation is evident in the small range of  $KD_1$  energy predictions  $(E_{KD_1} = 99(1), 81(0), 95(2) \text{ cm}^{-1}$  for  $[\mathbf{3}]_{Er_1}$ ,  $[\mathbf{3}]_{Er_2}$ ,  $[\mathbf{3}]_{Er_3}$ , respectively), when averaged between both

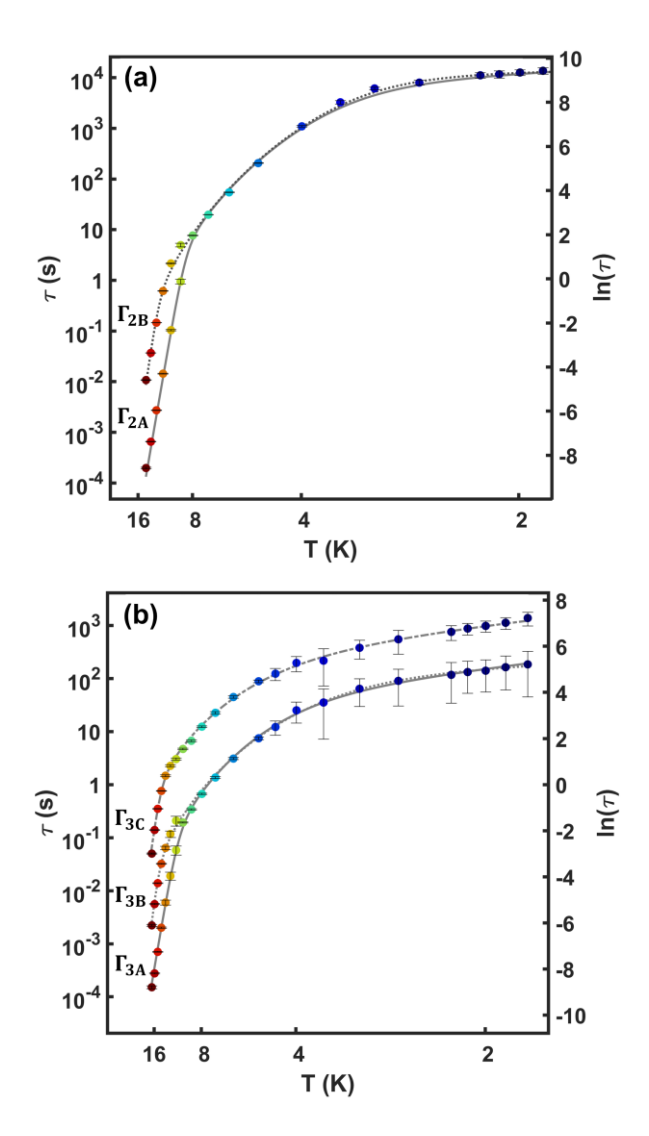


Figure 6. Arrhenius plots of relaxation times versus temperature for 2 (a, top) and 3 (b, bottom). Gray lines are fits to a multi-term relaxation model, Equation 7. For reference, in the text, each process ( $\Gamma$ ) is subscripted with the associated molecule (2-3) and indexed alphabetically from shortest to longest timescale. Error bars demonstrate upper and lower error limits of  $\tau$  values. Individual contributions from different processes are shown in Figures S35-S36 in the ESI.

fragments in the unit cell. In each case  $\theta$  remains predictive of the local axiality with minor cant angles predicted in spin-space  $(\theta_{cant,[3]_{1-3}} = 3.4^{\circ}, 6.5^{\circ}, 2.7^{\circ})$ . Note that while the single ion ground states  $(KD_0)$  of  $\mathbf{1}-\mathbf{3}$  are of nearly pure  $M_J = \pm 15/2$  composition, it is still preferrable to use the  $\alpha$  and  $\beta$  notation to avoid confusion between local and global spin orientations, and we will continue to utilize this notation in our discussion of the dipole doublets  $(DD_n)$  generated by POLY\_ANISO and introduced in the following section. This will become especially important in

the discussion of **3**, where three non-collinear spins must be tracked.

#### **DISCUSSION**

Relaxation dynamics in multinuclear lanthanide complexes has been a topic of interest since the first multi-nuclear Dv-based clusters were shown to display slow relaxation.<sup>43</sup> Unless coupling pathways are carefully engineered,44-47 single-ion effects remain dominant, due to the localized nature of the 4f orbitals. Although minor in terms of the overall energetics, the intramolecular magnetic coupling can induce a quantized molecular form of exchange biasing48 wherein the local magnetocrystalline anisotropy barrier is kept largely static, yet QTM pathways are drastically restructured. 49-51 Within this context, we will discuss the merits of describing 1-3 through the progressive perturbative approach summarized in Figure 1. This model allows for rationalization of exchange-biasing behavior as well as a surprisingly intuitive understanding of the low-energy magnetic manifolds of highly anisotropic, dipolar-coupled systems.

Critically, the behavior of **1** provides a magnetic building unit for descriptions of the more complex clusters, **2** – **3**. In **1**, the observation of a single-relaxation process with a transition from overbarrier ( $U_{eff} = 82(2) \text{ cm}^{-1}$ ) to through barrier relaxation at relatively fast timescales is consistent

with single-ion anisotropy of Er3+ with COT2ligation (Figure S32, Table S21). Interestingly, the relaxation dynamics of 1 closely mimic those of  $Er(COT)I(THF)_2$ ,  $(U_{eff} = 95 \text{ cm}^{-1})$ , indicating that any TiPS-induced perturbation of the ring electronic structure have negligible effect on the SMM properties. Within the context of our perturbative model, the ground Kramers doublet of **2**,  $KD_0$ , can be considered as the interaction of two high-purity  $M_I = \pm 15/2$  doublets via the magnetic dipole interaction. As observed via AC magnetic relaxation measurements, two temperaturedependent Orbach processes are present (T > 9 K;  $\Gamma_{2A}$  and  $\Gamma_{2B}$ , Figure 6). Below T = 9 K, the timescale of the AC resonance merges into a single process with sublinear Arrhenius temperature dependence indicative of Raman-type relaxation. Below T = 3 K, a region of linear temperature dependence is once again observed, with a large increase in the characteristic attempt time. To describe the low temperature relaxation barrier and to properly fit the dynamic magnetic data, we've implemented a second Arrhenius-type relaxation term in the multiterm relaxation equation typically used to fit magnetic data (Equation 7). Herein,  $D_{eff}$ , describes the dipolar barrier and  $\tau_D$ , the dipolar attempt time (analogous to  $U_{eff}$  and  $\tau_0$  at higher temperatures):

$$\tau^{-1} = \tau_0^{-1} exp\left(\frac{-U_{eff}}{k_B T}\right) + CT^n + \tau_D^{-1} exp\left(\frac{-D_{eff}}{k_B T}\right)$$
(Eq. 7)

		Fit (experimental)								
Compound	Process	$U_{eff}$ $(cm^{-1})$	$ au_0  ag{s}$	С	n	QTM		Calculated ( <i>ab initio</i> )		Predicted (empirical)
1	$\Gamma_{\!\scriptscriptstyle 1}$	82(2)	$4.6(7) \times 10^{-9}$	$2.5(8) \times 10^{-5}$	7.5(3)	$9.9(1) \times 10^{-3}$				
Compound	Process	$U_{eff}$ $(cm^{-1})$	$ au_0  ag{s}$	С	n	$D_{eff}$ $(cm^{-1})$	$\tau_D$ (s)	Dipole Doublet	$\Delta E_{calc} \ (\mathrm{cm}^{-1})$	$\Delta E_{pred} \ (\mathrm{cm}^{-1})$
2	$\Gamma_{2A}$	138(2)	$2.6(6) \times 10^{-10}$	$1.5(4) \times 10^{-7}$	6.7(2)	0.63(4)	$9.2(4) \times 10^3$	$DD_1$	0.65	0.62
	$\Gamma_{2B}$	152(1)	$2.5(3) \times 10^{-9}$	$8.7(6) \times 10^{-8}$	6.8(0)					
3	$\Gamma_{3A}$	139(1)	$1.3(1) \times 10^{-9}$	$4.0(0) \times 10^{-5}$	5.0(0)	0.26(5)	$1.5(5) \times 10^2$	$DD_1$	0.22	0.41
	$\Gamma_{3B}$	169(1)	$2.0(2) \times 10^{-9}$					$DD_2$	1.11	1.27
	$\Gamma_{3C}$	196(0)	$4.0(7) \times 10^{-9}$	$6.9(0) \times 10^{-6}$	4.5(0)	2.90(1)	$1.5(0) \times 10^{2}$	$DD_3$	2.83	2.79

Extraction of these parameters from the fitting of experimental relaxation data for **2** begins to shed light on the nature of the dipolar interaction, which brings about a small, low temperature dipolar relaxation barrier ( $D_{eff} = 0.63(4) \text{ cm}^{-1}$ ) and a lengthy dipolar attempt time ( $\tau_D = 9.2(4) \times 10^3 \text{ s}$ ; Table 1; ESI Section 3.4).

To further probe the viability of the dipole interaction as the defining perturbation controlling long-timescale magnetic dynamics, the splitting of the  $KD_0$  manifold by internuclear dipolar coupling was treated using the POLY\_ANISO module of OpenMolcas. The emergence of a weaklytemperature dependent linear region at low temperatures is consistent with the interpretation of a dipolar splitting to give new eigenstates (referred to here as dipole doublets,  $DD_n$ , to differentiate them from the rigorously degenerate single-ion Kramers doublets,  $KD_n$ ). overwhelmingly axial nature of the single-ion states  $(g_x = 0.0002; g_y = 0.0002; g_z = 17.9130)$  results in minimal mixing which is responsible for the doublet interpretation instead of the singlet-triplet formalism appropriate for interaction of isotropic

spin states. The nature and magnitude of the splitting of these states induced by the dipolar interaction is determined by the anisotropy of the single-ion moments and their collective projection onto the internuclear axis (Eq. 1) to yield a ferro- or antiferromagnetic coupling interaction. With a significant projection of the anisotropy axes in [2] onto the internuclear axis, the ground state is expected to correspond to the ferromagnetic orientation. We see this to be corroborated by the calculational output of POLY\_ANISO and the upturn in  $\gamma T$  vs. T in the static magnetic data (Figure 3): the ground state of [2] is associated with a largely ferromagnetic composition ( $DD_0$ ;  $M_Z = \pm 18$ ), and the excited dipole state  $(DD_1; M_Z = 0)$  with an antiferromagnetic composition (Figure Furthermore, the dipole splitting for a transition between the ground dipole doublet  $(DD_0)$  and the excited dipole doublet  $(DD_1)$  of [2] estimated from fitting the relaxation data  $(D_{eff} = 0.63(4) \text{ cm}^{-1})$ and that computed ab initio ( $\Delta E_{calc} = 0.65 \text{ cm}^{-1}$ ) are in excellent agreement (Figure 7, Table 1, Tables S14-15, S22-24). Excitingly, these data can also be interpreted via the real-space orientation of singleion anisotropy centers through a dipolar coupling

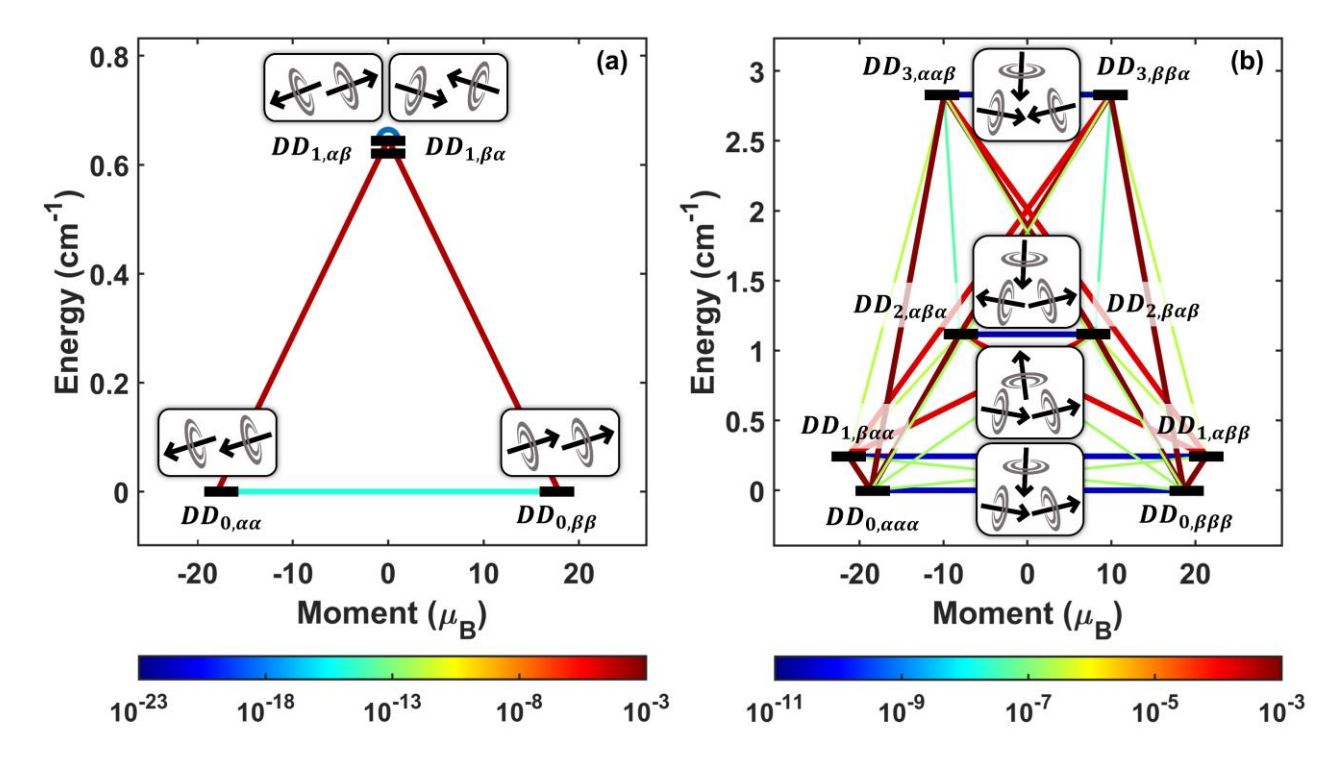


Figure 7. Calculated energy states of the magnetic dipole interaction Hamiltonian and representative Ising configurations for [2] and [3]. The Hamiltonian bases correspond to the four and eight pseudospin ½ single-ion states for [2] (a) and [3] (b), respectively. The g-factors were calculated at the CASSCF level. Ground and highest-excited state configurations for both species correspond to maximal net-ferromagnetic and net-antiferromagnetic interactions, respectively. Calculations were performed on structures with triisopropylsilyl groups replaced with hydrogen atoms. States are represented by black lines. Transverse magnetic moment elements (colored lines) are colored according to their magnitude (colorbar).  $\alpha$  and  $\beta$  are dipole doublet components related by time-reversal, as discussed in the text. Dipole components for [3] are labeled in order according to Figure 2, starting at the upper Er-1 center and progressing counter-clockwise:  $DD_{n.ET1.ET2.ET3}$ .

mechanism utilizing only two structural parameters. Thus, we can begin to understand, predict, and even design, dipolar interactions to drastically alter the nature of transitions between states without large perturbations to their energy.

A simple and intuitive calculation appears to be able to predict and approximate the nature of coupling present in **2**, utilizing only two crystallographically derived structural parameters: the internuclear erbium distance, r, and the angle,  $\theta$ , from the projection of the Er-COT vector  $(\vec{r}_{\perp})$  onto  $\vec{r}$ . Associating  $\vec{r}_{\perp}$  as the real-space indicator of the anisotropy axis yields a proportional, empirically-parameterized version of the dipolar equation:

$$E_{dip} = -\frac{\mu_B^2 \mu^2}{r^3} [3\cos\theta_1 \cos\theta_2 - \cos(\Delta\theta)]$$
(Eq. 8)

In these pair-wise dipolar interactions,  $\theta_1$  and  $\theta_2$ are angles from the projections of moment onto the internuclear axis.  $\Delta \theta$  is the difference between angles  $\theta_1$  and  $\theta_2$ , and r is the magnitude of the internuclear vector. For example, when  $\theta_1 = \theta_2 =$ 0°, a maximally ferromagnetically coupled ground state is obtained, whereas when  $\theta_1$  = 0° and  $\theta_2$  = 180° the antiferromagnetically coupled state is favored. Sample calculations, figures, and angle tabulations are provided in section 3.2 of the ESI. Use of our experimental data without further parameterization (Tables S1, S3, Figure S4), predicts that 2 will have a ferromagnetically dipolar ground state and coupled antiferromagnetically coupled dipolar excited state. Scaling the experimentally derived data by values expected for an anisotropic erbium(III), predicts these states to be split by 0.62 cm<sup>-1</sup>, a value surprisingly consistent with experimentally fit  $(D_{eff} = 0.63(4) \text{ cm}^{-1})$  and calculated  $(0.65 \text{ cm}^{-1})$  given the simplicity of the model (Table 1; Section 3.2 of ESI). This quick and simple calculation becomes an excellent first-order approximation of expected dipolar coupling in such with the propensity of systems saving computational costs and increasing chemical intuition towards synthetic strategies. It also promises predictive capability in far more complex systems where multiple interactions and distances must be accounted for, and highly complex spin structures may emerge.

Further analysis of the transition matrix elements of the ab initio calculated dipole-coupled states

offers more insight into the length of relaxation times in the low-temperature regime. Dipolar coupling brings about significantly lower transition probabilities between opposite spin polarizations of the lowest energy dipolar-coupled state:

$$DD_{0,\alpha\alpha} \xrightarrow{10^{-15}} DD_{0,\beta\beta} \ (Eq.9)$$

with those of thermally assisted QTM transitions diminished by a further 6 orders of magnitude (Table S13):

$$DD_{1,\alpha\beta} \xrightarrow{\stackrel{10^{-21}}{\longleftarrow}} DD_{1,\beta\alpha} \ (Eq. 10).$$

This dramatic suppression of the QTM relaxation pathway can be equated with the reduction in probability for simultaneously flipping both spins (indicated by icons in Figure 7), consequently leading to an increased dipolar attempt time ( $\tau_D = 9.2(4) \times 10^3$  s; Table 1). The low probability of QTM transitions in [2] shuttle magnetic relaxation over the dipole relaxation barrier, a two-step process in which each step can be thought of as roughly analogous to the flip of a single spin. Despite being a two-step, thermally activated process, the low barrier and lack of alternate pathways leave:

$$DD_{0,\alpha\alpha} \stackrel{\longleftarrow}{\longleftrightarrow} DD_{0,\alpha\beta} \stackrel{10^{-4}}{\longleftrightarrow} DD_{0,\beta\beta} (Eq.11)$$

as the most prominent pathway for low temperature relaxation. This mechanism is consistent with the residual temperature dependence observed in the time-dependent magnetic susceptibility, even at the lowest temperatures (Figure 6). Note that the state  $DD_{0,\beta\alpha}$  provides an equivalent intermediate for the two-step pathway of Eq. 11. In such cases of equivalence, the relaxation will be discussed in terms of the majority  $\alpha$  to majority  $\beta$  pathway.

To summarize, we consider the dipolar coupling as a perturbation on the crystal field states, splitting them into a tight manifold composed of linear combinations of the single-ion  $M_J$  states nearest in energy (Figure 1). By this formalism, the splitting of the crystal field  $(M_J)$  manifold under the intramolecular dipolar perturbation becomes a consistent and intuitive predictor of the long-timescale relaxation pathway. For [2], Equations 9

 $(DD_0)$  and 10  $(DD_1)$  both depict transitions between states differing by two spin-flips. The parallel spatial orientation of the anisotropy axes in relation to each other and the internuclear vector ensures that  $DD_0$  (the bistable ferromagnetic state) is lower in energy than  $DD_1$  (the antiferromagnetic state). Due to the spatial arrangement and high state-purity, both of these transitions have very low probabilities. Alternatively, Equation 11 depicts the preferred two-step, thermally activated transition wherein each step flips a single Ising spin.

The hierarchical approach to perturbation analysis used to understand 2 allows us to tackle the far more complicated relaxation dynamics of 3. Experimentally, three relaxation processes can be observed and tracked above  $T = 11 \text{ K} (\Gamma_{3A-C}, \text{ Figure})$ 6). As observed in 2,  $\Gamma_{3A,B}$  merge and exhibit a secondary regime of Arrhenius behavior at low temperatures. Alternatively,  $\Gamma_{3C}$  is offset from  $\Gamma_{3AB}$ , exhibiting its own Orbach, Raman, and dipole regions. As with 2, we can attribute the weakly temperature-dependent region to dipolar coupling and begin our analysis by calculating a dipole energy manifold based on the dipolar interactions between  $KD_0$  of all three ions (Figure 7b). The coupling interaction manifold of [3] shows the presence of four different dipole doublets with excited states  $(DD_{1-3})$  above the ground state at energies of 0.22, 1.11, and 2.83 cm<sup>-1</sup>, respectively (Figure 7b, Table 1).  $DD_0$  and  $DD_1$  have the largest  $M_Z = \pm 19 \text{ and } \pm 21 \,\mu_B$ moments with respectively, and represent the ferromagnetically coupled states (Eq. 12).  $DD_2$  and  $DD_3$  represent the net-antiferromagnetically coupled states at  $M_Z = \pm 8$  and  $\pm 10 \mu_B$ . The transition matrix elements span a wide range, with the most probable single-step transitions from the ground state corresponding to:

$$DD_{0,\alpha\alpha\alpha} \xrightarrow{\stackrel{10^{-3}}{\longleftarrow}} DD_{1,\beta\alpha\alpha} (Eq. 12),$$

$$DD_{0,\alpha\alpha\alpha} \xrightarrow{\stackrel{10^{-4}}{\longleftarrow}} DD_{2,\alpha\beta\alpha} (Eq. 13),$$

and

$$DD_{0,\alpha\alpha\alpha} \stackrel{\stackrel{10^{-4}}{\longleftarrow}}{\longrightarrow} DD_{3,\alpha\alpha\beta} (Eq. 14)$$

These three processes correspond to single-step, single-flip transitions from the ground dipole doublet to each excited dipole doublet. Interestingly, two of these calculated processes

correspond to experimentally observed relaxation processes. When the time scales of  $\Gamma_{3A}$  and  $\Gamma_{3B}$ merge at low temperatures,  $D_{eff}$  is fit to give a dipolar barrier of 0.26(5) cm<sup>-1</sup>. This corresponds well with the calculated energy splitting between  $DD_0$  and  $DD_1$  (Eq. 12) of  $\Delta E_{calc} = 0.22 \text{ cm}^{-1}$ (Figure 7b, Tables 1, S19-20, S25-S28). Analogously, the low temperature transition of  $\Gamma_{3C}$  corresponds to the single-flip transition encompassing the whole dipole manifold (Eq. 14). The calculated energy splitting is still consistent between the model and experimental data ( $D_{eff} = 2.90(1) \text{ cm}^{-1}$ ;  $\Delta E_{calc} =$ 2.83 cm<sup>-1</sup>). Once again, our model wherein the energy levels are derived using two simple crystallographic parameters, r and  $\theta$ , provides a satisfactory prediction of the net coupling type and energy splitting:  $DD_0$ , FM;  $DD_1$ , FM,  $\Delta E_{pred} =$ 0.41 cm<sup>-1</sup>;  $DD_2$ , AFM,  $\Delta E_{pred} = 1.27 \text{ cm}^{-1}$ ;  $DD_3$ , AFM,  $\Delta E_{nred} = 2.79 \text{ cm}^{-1}$  (Table 1, ESI section 3.2).

The dipole attempt times for processes  $\Gamma_{3A/B}$  and  $\Gamma_{3C}$  are  $\tau_D = 1.5(5) \times 10^2$  and  $1.5(0) \times 10^2$  s, respectively, comparatively lower than those observed in 2. The difference is due in part to the triangular structure of 3, where two of the interacting spins are near-linear with respect to each other, with the third oriented in a nearorthogonal configuration to the other two. This is clearly evident in the spin configuration between  $DD_0$  and  $DD_1$  (Figure S5), where erbium centers  $[3]_{Er_2}$  and  $[3]_{Er_3}$  have major projections onto their internuclear axis and are ferromagnetically, whereas erbium center  $[3]_{Er_1}$ offers a minimal contribution to net coupling. Furthermore, the dipolar manifold of [3] offers two evident pathways to relaxation (Eqs. 12, 14) and the increased mixing of states due to lowered symmetry of dipolar interactions may also play a role in decreased relaxation times.

As in [2], the logic of correlating transition probability with the number of anisotropic spin flips can be carried throughout the entire manifold of [3], with the highest-probability transitions corresponding to single-flip transitions, followed by two-flip transitions, and the lowest-probability transitions corresponding to the three-flip transitions (Table S20):

$$DD_{n,\alpha\alpha\alpha} \stackrel{\stackrel{10^{-12}}{\longleftarrow}}{\longrightarrow} DD_{n,\beta\beta\beta} (Eq.15)$$

The relationship between anisotropic spin flips and transition probability continues to build upon the intuitive model of dipolar relaxation that could be further applied to multinuclear magnetic complexes with strongly anisotropic spins.

# CONCLUSION

We have targeted systems that highlight dipolar coupling as a driving factor in controlling magnetic relaxation. Beginning with a mononuclear unit of stable magnetic anisotropy, we synthesized a series erbium(III) single-molecule magnets increasing nuclearity to investigate the relaxation dynamics of di- and tri-nuclear erbium(III) systems in the high and low temperature regimes. Broadly speaking, the ability to generate and rationalize the low-energy magnetic manifolds as demonstrated for 1-3 points to strongly anisotropic molecular magnetic dipoles as an underexploited approach to fine-tune the design of n-dimensional (n = 0-3) spin structures with unprecedented levels of complexity. The existence and properties of a ferromagnetic ground state are made possible by tracking the multi-relaxation behavior through resonant interaction with an AC magnetic field across eight orders of magnitude in frequency space. In doing so, two and three concurrent relaxation pathways are uncovered in the high-temperature regime for the di- and trinuclear species, respectively. When fit to a multi-term relaxation model, a second Arrhenius law-regime is revealed at low temperatures, corresponding to the dynamics of the dipole coupled states within the ground Kramers doublet manifold. Calculation of the Kramers doublet structure and dipolar interactions provide a preliminary quantitative basis for rationalizing the relaxation pathways. In correspondence with ab initio calculations, dipolar coupling suppresses OTM relaxation in the low-temperature regime by forcing through-barrier relaxation transitions to take place between the coupled dipole doublet states and is thus the driving factor to elongated relaxation times. The anisotropic states and dipolar mechanism provide an intuitive framework single-spin whereby anisotropic flips preferential per each step in a transition through the dipole barrier and QTM is suppressed as it requires the simultaneous flip of every spin in the system. Additionally, the type of coupling and approximate dipolar energy splitting can be predicted through a simple calculation involving only two crystallographically-derived physical parameters. We plan to use the predictive nature of design in these anisotropic dipolar manifolds as a basis for a wide array of exciting directions including higher and more complex symmetries, increased dimensionality, and exploration of the intrinsic quantum properties of the dipole manifolds.

# **ASSOCIATED CONTENT**

# Supporting Information

This material is available free of charge via the Internet at <a href="http://pubs.acs.org">http://pubs.acs.org</a>.

Preparative details, sample characterization, physical and computational details for all compounds, equations S1-S3, figures S1-S36, tables S1-S30 (PDF).

# **AUTHOR INFORMATION**

Corresponding Author \*jrinehart@ucsd.edu

#### ORCID

Angelica P. Orlova: 0000-0002-2446-1384 Jeremy D. Hilgar: 0000-0001-5142-3079 Maximilian G. Bernbeck: 0000-0001-6329-5860 Milan Gembicky: 0000-0002-3898-1612 Jeffrey D. Rinehart: 0000-0002-5478-1995

#### Notes

The authors declare no competing financial interest.

### **ACKNOWLEDGMENT**

This research was funded through the National Science Foundation Division of Materials Research #1904937 and in part under the NSF-AGEP supplement award. We are thankful to the W. M. Keck Laboratory for Integrated Biology for time on their supercomputer; the UCSD Crystallography Facility; to the Figueroa Group, in particular Krista P. Balto, for the use of their FT-IR; and Jacques P. Coulombe for stimulating and helpful discussions.

#### **REFERENCES**

- (1) Rinehart, J. D.; Long, J. R. "Exploiting single-ion anisotropy in the design of f-element single-molecule magnets" *Chem Sci* **2011**, *2*, 2078. (2) Woodruff, D. N.; Winpenny, R. E. P.; Layfield, R. A. "Lanthanide
- (2) Woodruff, D. N.; Winpenny, R. E. P.; Layfield, R. A. "Lantha Single-Molecule Magnets" *Chemical Reviews* **2013**, *113*, 5110.
- (3) Jackson, C. E.; Moseley, I. P.; Martinez, R.; Sung, S.; Zadrozny, J. M. "A reaction-coordinate perspective of magnetic relaxation" *Chemical Society Reviews* **2021**, *50*, 6684.
- (4) Christou, G.; Gatteschi, D.; Hendrickson, D. N.; Sessoli, R. "Single-Molecule Magnets" *MRS Bulletin* **2000**, *25*, 66.
- (5) Guo, F. S.; Day, B. M.; Chen, Y. C.; Tong, M. L.; Mansikkamaki, A.; Layfield, R. A. "Magnetic hysteresis up to 80 kelvin in a dysprosium metallocene single-molecule magnet" *Science* **2018**, *362*, 1400.
- (6) Ding, Y.-S.; Yu, K.-X.; Reta, D.; Ortu, F.; Winpenny, R. E. P.; Zheng, Y.-Z.; Chilton, N. F. "Field- and temperature-dependent quantum tunnelling of the magnetisation in a large barrier single-molecule magnet" *Nature Communications* **2018**, *9*, 3134.
- (7) Gómez-Coca, S.; Urtizberea, A.; Cremades, E.; Alonso, P. J.; Camón, A.; Ruiz, E.; Luis, F. "Origin of slow magnetic relaxation in Kramers ions with non-uniaxial anisotropy" *Nature Communications* **2014**, *5*, 4300.

- (8) Lunghi, A.; Totti, F.; Sanvito, S.; Sessoli, R. "Intra-molecular origin of the spin-phonon coupling in slow-relaxing molecular magnets" *Chem Sci* **2017**, *8*, 6051.
- (9) Moseley, D. H.; Stavretis, S. E.; Zhu, Z.; Guo, M.; Brown, C. M.; Ozerov, M.; Cheng, Y.; Daemen, L. L.; Richardson, R.; Knight, G.; Thirunavukkuarasu, K.; Ramirez-Cuesta, A. J.; Tang, J.; Xue, Z.-L. "Inter-Kramers Transitions and Spin-Phonon Couplings in a Lanthanide-Based Single-Molecule Magnet" *Inorganic Chemistry* **2020**, *59*, 5218.
- (10) Liu, J.-L.; Chen, Y.-C.; Tong, M.-L. "Symmetry strategies for high performance lanthanide-based single-molecule magnets" *Chemical Society Reviews* **2018**, *47*, 2431.
- (11) Bernbeck, M. G.; Hilgar, J. D.; Rinehart, J. D. "Probing axial anisotropy in dinuclear alkoxide-bridged Er-COT single-molecule magnets" *Polyhedron* **2020**, *175*, 114206.
- (12) Hilgar, J. D.; Bernbeck, M. G.; Flores, B. S.; Rinehart, J. D. "Metalligand pair anisotropy in a series of mononuclear Er-COT complexes" *Chem Sci* **2018**, *9*, 7204.
- (13) Hilgar, J. D.; Bernbeck, M. G.; Rinehart, J. D. "Million-fold Relaxation Time Enhancement across a Series of Phosphino-Supported Erbium Single-Molecule Magnets" *J Am Chem Soc* **2019**, *141*, 1913.
- (14) Hilgar, J. D.; Butts, A. K.; Rinehart, J. D. "A method for extending AC susceptometry to long-timescale magnetic relaxation" *Phys Chem Chem Phys* **2019**, *21*, 22302.
- (15) Hilgar, J. D.; Flores, B. S.; Rinehart, J. D. "Ferromagnetic coupling in a chloride-bridged erbium single-molecule magnet" *Chem Commun* **2017**, *53*, 7322.
- (16) Meng, Y.-S.; Yang, M.-W.; Xu, L.; Xiong, J.; Hu, J.-Y.; Liu, T.; Wang, B.-W.; Gao, S. "Design principle of half-sandwich type erbium single-ion magnets through crystal field engineering: a combined magnetic and electronic structure study" *Dalton Transactions* **2019**, *48*, 10407.
- (17) Lu, G.; Liu, Y.; Deng, W.; Huang, G.-Z.; Chen, Y.-C.; Liu, J.-L.; Ni, Z.-P.; Giansiracusa, M.; Chilton, N. F.; Tong, M.-L. "A perfect triangular dysprosium single-molecule magnet with virtually antiparallel Ising-like anisotropy" *Inorganic Chemistry Frontiers* **2020**, *7*, 2941.
- (18) Trambitas, A. G.; Yang, J. Y.; Melcher, D.; Daniliuc, C. G.; Jones, P. G.; Xie, Z. W.; Tamm, M. "Synthesis and Structure of Rare-Earth-Metal Dicarbollide Complexes with an Imidazolin-2-iminato Ligand Featuring Very Short Metal-Nitrogen Bonds" *Organometallics* **2011**, *30*, 1122.
- (19) Cendrowski-Guillaume, S. M.; Le Gland, G.; Nierlich, M.; Ephritikhine, M. "Lanthanide Borohydrides as Precursors to Organometallic Compounds. Mono(cyclooctatetraenyl) Neodymium Complexes" *Organometallics* **2000**, *19*, 5654.
- (20) Mashima, K.; Shibahara, T.; Nakayama, Y.; Nakamura, A. "Mononuclear η8-cyclooctatetraenyl(thiolato)samarium(III) complexes (η8-C8H8)Sm(SR)(hmpa)2 (R=2,4,6-triisopropylphenyl and 2-pyridyl; HMPA=hexamethylphosphoric triamide) derived from metallic samarium, diaryl disulfide, and 1,3,5,7-cyclooctatetraene in the" Journal of Organometallic Chemistry 1998, 559, 197.
- (21) Hodgson, K. O.; Raymond, K. N. "Dimeric .pi.-cyclooctatetraene dianion complex of cerium(III). Crystal and molecular structure of [Ce(C8H8)Cl.20C4H8]2" *Inorganic Chemistry* **1972**, *11*, 171.
- (22) Hilgar, J. D.; Bernbeck, M. G.; Flores, B. S.; Rinehart, J. D. "Metalligand pair anisotropy in a series of mononuclear Er–COT complexes" *Chem Sci* **2018**, *9*, 7204.
- (23) Wayda, A. L.; Mukerji, I.; Dye, J. L.; Rogers, R. D. "Divalent lanthanoid synthesis in liquid ammonia. 2. The synthesis and x-ray crystal structure of (C8H8)Yb(C5H5N)3.1/2C5H5N" *Organometallics* **1987**, *6*, 1328.
- (24) Mashima, K.; Fukumoto, H.; Nakayama, Y.; Tani, K.; Nakamura, A. "Cationic monocyclooctatetraenyl-lanthanoid complexes derived from metallic lanthanoid: crystal structures of [Sm( $\eta$ 8-C8H8)(hmpa)3]I and [Sm( $\eta$ 8-C8H8)(hmpa)3][Sm( $\eta$ 8-C8H8)2] (HMPA = hexamethylphosphoric triamide)" *Polyhedron* **1998**, *17*, 1065.
- (25) Edelmann, A.; Lorenz, V.; Hrib, C. G.; Hilfert, L.; Blaurock, S.; Edelmann, F. T. "Steric Effects in Lanthanide Sandwich Complexes Containing Bulky Cyclooctatetraenyl Ligands" *Organometallics* **2013**, *32*, 1435.
- (26) Meermann, C.; Ohno, K.; Törnroos, K. W.; Mashima, K.; Anwander, R. "Rare-Earth Metal Bis(dimethylsilyl)amide Complexes Supported by Cyclooctatetraenyl Ligands" *European Journal of Inorganic Chemistry* **2009**, *2009*, 76.
- (27) Roesky, P. W.; Gamer, M. T.; Marinos, N. "Yttrium and Lanthanide Diphosphanylamides: Syntheses and Structures of Complexes with

- one{(Ph2P)2N}- ligand in the Coordination Sphere" *Chemistry A European Journal* **2004**, *10*, 3537.
- (28) Harriman, K. L. M.; Korobkov, I.; Murugesu, M. "From a Piano Stool to a Sandwich: A Stepwise Route for Improving the Slow Magnetic Relaxation Properties of Thulium" *Organometallics* **2017**, *36*, 4515.
- (29) Visseaux, M.; Nief, F.; Ricard, L. "Synthesis of mixed phospholyl/cyclooctatetraenyl-lanthanide complexes. Crystal and molecular structure of (cyclooctatetraenyl)[3,4-dimethyl-2,5-bis(trimethylsilyl)-phospholyl](tetrahydrofuran)neodymium" *Journal of Organometallic Chemistry* **2002**, *647*, 139.
- (30) Kahn, O. Molecular Magnetism; VCH Publishers, Inc., 1993.
- (31) Gatteschi, D.; Sessoli, R.; Villain, J. "Molecular Nanomagnets" *Mesoscopic Phys Nano* **2006**, 1, 71.
- (32) Guo, Y.-N.; Xu, G.-F.; Gamez, P.; Zhao, L.; Lin, S.-Y.; Deng, R.; Tang, J.; Zhang, H.-J. "Two-Step Relaxation in a Linear Tetranuclear Dysprosium(III) Aggregate Showing Single-Molecule Magnet Behavior" *J Am Chem Soc* **2010**, *132*, 8538.
- (33) Guo, Y.-N.; Xu, G.-F.; Wernsdorfer, W.; Ungur, L.; Guo, Y.; Tang, J.; Zhang, H.-J.; Chibotaru, L. F.; Powell, A. K. "Strong Axiality and Ising Exchange Interaction Suppress Zero-Field Tunneling of Magnetization of an Asymmetric Dy2 Single-Molecule Magnet" *J Am Chem Soc* **2011**, *133*, 11948.
- (34) Ho, L. T. A.; Chibotaru, L. F. "Multiple relaxation times in single-molecule magnets" *Phys Rev B* **2016**, *94*, 104422.
- (35) Fdez. Galván, I.; Vacher, M.; Alavi, A.; Angeli, C.; Aquilante, F.; Autschbach, J.; Bao, J. J.; Bokarev, S. I.; Bogdanov, N. A.; Carlson, R. K.; Chibotaru, L. F.; Creutzberg, J.; Dattani, N.; Delcey, M. G.; Dong, S. S.; Dreuw, A.; Freitag, L.; Frutos, L. M.; Gagliardi, L.; Gendron, F.; Giussani, A.; González, L.; Grell, G.; Guo, M.; Hoyer, C. E.; Johansson, M.; Keller, S.; Knecht, S.; Kovačević, G.; Källman, E.; Li Manni, G.; Lundberg, M.; Ma, Y.; Mai, S.; Malhado, J. P.; Malmqvist, P. Å.; Marquetand, P.; Mewes, S. A.; Norell, J.; Olivucci, M.; Oppel, M.; Phung, Q. M.; Pierloot, K.; Plasser, F.; Reiher, M.; Sand, A. M.; Schapiro, I.; Sharma, P.; Stein, C. J.; Sørensen, L. K.; Truhlar, D. G.; Ugandi, M.; Ungur, L.; Valentini, A.; Vancoillie, S.; Veryazov, V.; Weser, O.; Wesołowski, T. A.; Widmark, P.-O.; Wouters, S.; Zech, A.; Zobel, J. P.; Lindh, R. "OpenMolcas: From Source Code to Insight" Journal of Chemical Theory and Computation 2019, 15, 5925.
- (36) Aquilante, F.; Autschbach, J.; Baiardi, A.; Battaglia, S.; Borin, V. A.; Chibotaru, L. F.; Conti, I.; De Vico, L.; Delcey, M.; Fdez. Galván, I.; Ferré, N.; Freitag, L.; Garavelli, M.; Gong, X.; Knecht, S.; Larsson, E. D.; Lindh, R.; Lundberg, M.; Malmqvist, P. Å.; Nenov, A.; Norell, J.; Odelius, M.; Olivucci, M.; Pedersen, T. B.; Pedraza-González, L.; Phung, Q. M.; Pierloot, K.; Reiher, M.; Schapiro, I.; Segarra-Martí, J.; Segatta, F.; Seijo, L.; Sen, S.; Sergentu, D.-C.; Stein, C. J.; Ungur, L.; Vacher, M.; Valentini, A.; Veryazov, V. "Modern quantum chemistry with [Open]Molcas" *The Journal of Chemical Physics* **2020**, *152*, 214117.
- (37) Chibotaru, L. F.; Ungur, L.; Soncini, A. "The Origin of Nonmagnetic Kramers Doublets in the Ground State of Dysprosium Triangles: Evidence for a Toroidal Magnetic Moment" *Angewandte Chemie International Edition* **2008**, *47*, 4126.
- (38) Liebschner, D.; Afonine, P. V.; Urzhumtsev, A. G.; Adams, P. D. "Implementation of the riding hydrogen model in CCTBX to support the next generation of X-ray and neutron joint refinement in Phenix" *Method Enzymol* **2020**, *634*, 177.
- (39) Sheldrick, G. M.; Schneider, T. R. "SHELXL: High-resolution refinement" *Macromolecular Crystallography, Pt B* **1997**, *277*, 319.
- (40) Le Roy, J. J.; Korobkov, I.; Murugesu, M. "A sandwich complex with axial symmetry for harnessing the anisotropy in a prolate erbium(iii) ion" *Chem. Commun.* **2014**, *50*, 1602.
- (41) Le Roy, J. J.; Ungur, L.; Korobkov, I.; Chibotaru, L. F.; Murugesu, M. "Coupling Strategies to Enhance Single-Molecule Magnet Properties of Erbium-Cyclooctatetraenyl Complexes" *J Am Chem Soc* **2014**, *136*, 8003
- (42) Ungur, L.; Thewissen, M.; Costes, J.-P.; Wernsdorfer, W.; Chibotaru, L. F. "Interplay of Strongly Anisotropic Metal Ions in Magnetic Blocking of Complexes" *Inorganic Chemistry* **2013**, *52*, 6328. (43) Lin, P. H.; Korobkov, I.; Wernsdorfer, W.; Ungur, L.; Chibotaru, L. F.; Murugesu, M. "A Rare mu(4)-O Centred Dy-4 Tetrahedron with Coordination-Induced Local Chirality and Single-Molecule Magnet
- Behaviour" *European Journal of Inorganic Chemistry* **2011**, 1535. (44) Demir, S.; Gonzalez, M. I.; Darago, L. E.; Evans, W. J.; Long, J. R. "Giant coercivity and high magnetic blocking temperatures for N2 3–radical-bridged dilanthanide complexes upon ligand dissociation"

Nature Communications 2017, 8, 2144.

- (45) Mavragani, N.; Errulat, D.; Gálico, D. A.; Kitos, A. A.; Mansikkamäki, A.; Murugesu, M. "Radical-Bridged Ln 4 Metallocene Complexes with Strong Magnetic Coupling and a Large Coercive Field" *Angewandte Chemie International Edition* **2021**, *60*, 24206.
- (46) Rinehart, J. D.; Fang, M.; Evans, W. J.; Long, J. R. "Strong exchange and magnetic blocking in N23–-radical-bridged lanthanide complexes" *Nature Chemistry* **2011**, *3*, 538.
- (47) Rinehart, J. D.; Fang, M.; Evans, W. J.; Long, J. R. "A N23–Radical-Bridged Terbium Complex Exhibiting Magnetic Hysteresis at 14 K" *J Am Chem Soc* **2011**, *133*, 14236.
- (48) Coey, J. M. D. *Magnetism and Magnetic Materials*; Cambridge University Press: Cambridge, 2010.
- (49) Dolai, M.; Moreno-Pineda, E.; Wernsdorfer, W.; Ali, M.; Ghosh, A. "Exchange-Bias Quantum Tunneling of the Magnetization in a

- Dysprosium Dimer" *The Journal of Physical Chemistry A* **2021**, *125*, 8230.
- (50) Ghosh, T.; Marbey, J.; Wernsdorfer, W.; Hill, S.; Abboud, K. A.; Christou, G. "Exchange-biased quantum tunnelling of magnetization in a [Mn3]2 dimer of single-molecule magnets with rare ferromagnetic inter-Mn3 coupling" *Phys Chem Chem Phys* **2021**, *23*, 8854.
- (51) Han, T.; Giansiracusa, M. J.; Li, Z. H.; Ding, Y. S.; Chilton, N. F.; Winpenny, R. E. P.; Zheng, Y. Z. "Exchange-Biasing in a Dinuclear Dysprosium(III) Single-Molecule Magnet with a Large Energy Barrier for Magnetisation Reversal" *Chemistry A European Journal* **2020**, *26*, 6773.

# TOC Graphic

